Energy and Buildings 162 (2018) 121–133

Contents lists available at ScienceDirect

Energy and Buildings

journal homepage: www.elsevier.com/locate/enbuild

Characterization and data-driven modeling of a retro-reflective coating in RADIANCE

Lars O. Grobe

Lucerne University of Applied Sciences and Arts, 6048 Horw, Switzerland

ARTICLE INFO

Article history:
Received 17 August 2017
Received in revised form
15 December 2017
Accepted 17 December 2017
Available online 18 December 2017

Keywords:
Retro-reflection
Daylight simulation
Data-driven model
BSDF
Shading
Glare
Radiance
Complex fenestration

ABSTRACT

Retro-reflective coatings applied to blinds of reduced geometric complexity promise to provide view to the outside while effectively controlling solar gains and glare. To characterize the reflection characteristics of such coatings over the entire solar spectrum, a novel extension to a scanning gonio-photometer is developed. The extended instrument is tested and applied to measure a coating's Bidirectional Reflection Distribution Function including the region of the retro-reflected peak. The measured datasets are compiled into a data-driven reflection model for the daylight simulation software RADIANCE. This model is applied to illustrate the coating's effect in a comparison to purely diffuse and specular surface finishes on geometrically identical, flat blinds. Daylight supply, the probability of glare, and solar gains are assessed for an exemplary, South-oriented office under sunny sky conditions. The results indicate the potential of the coating to effectively shade direct sunlight even if applied on blinds with minimalistic geometries. The modeling technique is shown to be a general means to replicate the irregular optical properties of the coating, which cannot be represented by the standard models in daylight simulation software.

1. Introduction

1.1. Background and objectives

The effective shading of direct sunlight is a key requirement for fenestration systems aiming for high thermal and visual performance. Solar gains shall be avoided at most times to prevent over-heating effects in well-insulated buildings. Exposure to direct sunlight, while desirable to a certain degree in residential buildings [1], can cause discomfort and veiling glare and severely affect the visual comfort e.g. in offices. Yet the supply of daylight and a view to the outside are essential performance criteria in facade design since they address energy efficiency targets as well as the comfort and well-being of occupants [2,3].

Venetian blinds comprising profiles of often high geometric complexity address the dilemma to minimize the obstruction of view and daylight aperture, but exclude sunlight from being transmitted directly or by reflections in the fenestration [4,5]. However, the use of simple geometries appears to be desirable for at least two reasons. First, the manufacturing process to produce blinds with complex profiles is elaborate, if low tolerances shall be maintained. Second, any profile deviating from an ideal, flat slat occludes the view to the outside.

As an innovative approach to decouple shading performance from profile geometry, the application of a retro-reflective coating to the slats of Venetian blinds, and its effect on the daylight supply to an attached office, shall be tested.

1.2. Retro-reflection

Retro-reflection forms a special case of irregular light scattering by devices that "reflect incident light back toward the direction of the light source, operating over a wide range of angles of incidence" [6,pp. 31–32]. The effect is utilized in a range of applications such as traffic signs and reflectors attached e.g. to clothes enhancing visibility.

When applied to complex fenestration systems (CFS), the term retro-reflection is often used in a broader sense, including devices that deflect light by altering only the elevation angle [7,8]. Since the horizontal azimuth angle is not affected by such CFSs, retro-reflection according to the formal definition given above occurs

Abbreviations: BS, beam splitter; BSDF, Bidirectional Scattering distribution function; CBDM, climate-based daylight modeling; CFS, complex fenestration system; DGI, Daylight Glare Index; DGP, Daylight Glare Probability; DSF, differential scattering function; IGDB, International Glazing Database; NIr, near infrared light 780–2500 nm; sDA, spatial Daylight Autonomy; SHGC, solar heat gain coefficient; Vis, visible light 380–780 nm; XML, extensible markup language.

E-mail address: larsoliver.grobe@hslu.ch

https://doi.org/10.1016/j.enbuild.2017.12.029

Fig. 1. A naive approach to measure retro-reflection leads to shading by the detector.

only for one given cardinal direction. Examples are retro-reflecting blinds, formed by extrusion of two-dimensional profiles. Such slats with configurable inclination angle are employed in CFSs to block direct sunlight. Complex profile geometries, combining sections that retro-reflect light from potential incident sun directions with sections that deflect light upward, allow to balance the daylight supply from direct sunlight with solar gains. The application of small-scale prismatic structures achieves retro-reflection even with simple geometries such as extruded arcs [9,10].

The use of retro-reflective coatings comprising spherical and prismatic micro-structures in buildings has been proposed to mitigate urban heat islands effects [11,12]. A transparent window film applying such prismatic micro-structures has been demonstrated to selectively retro-reflect incident sunlight from high elevation [13].

Applied on the surface of Venetian blinds, retro-reflective coatings have the potential to meet high visual and thermal comfort targets even with simple geometric profiles according to ray-tracing based assessments [14]. Empirical methods are however required to account for effects caused by imperfections in the composition and application of coatings [15], and if the effective micro-structure is unknown or cannot be disclosed.

1.3. Measurement techniques

In typical configurations for reflection measurements, the retro-reflected fraction of scattered light is assumed to be negligible and excluded. An indirect measurement of this retro-reflected fraction by comparing absorption derived from calorimetric measurements with radiometric measurements of diffuse reflection has been proposed as an approximation [16].

A more comprehensive description of the directional distribution of retro-reflected light can be expressed by the Bidirectional Scattering distribution function (BSDF), describing the radiative flux between any pair of incident and outgoing scattered direction [17–20]. However, such directionally resolved characterization of retro-reflection employing gonio-photometers is a particular challenge, since light source and detector occlude each other if incident and outgoing direction are close to equal (Fig. 1). Only a very long distance between sample and detector allows to cover the peak region of highly directional retro-reflection in such direct measurements [21].

The introduction of a plate beam splitter (BS) between light source and sample allows the gonio-photometric measurement of

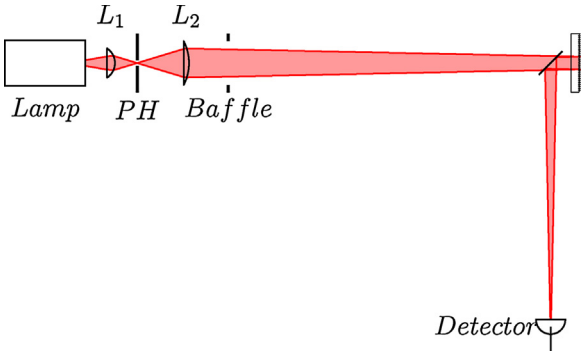

Fig. 2. Configuration employing one beam-splitter.

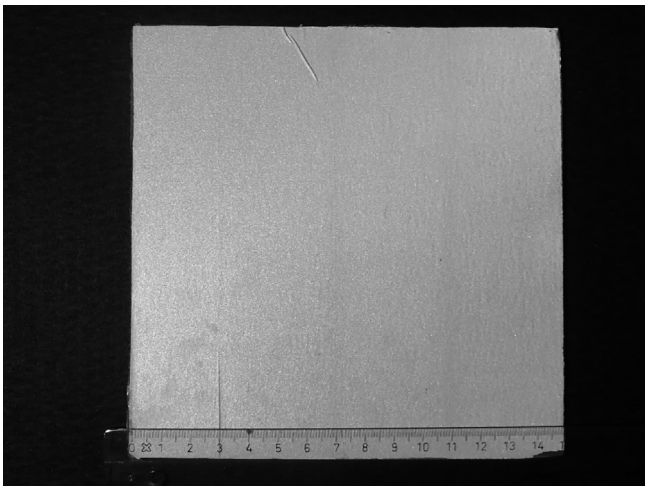

Fig. 3. Sample for the measurement of the retro-reflective BSDF. The coating is applied on a 150 mm × 150 mm metal sheet, which is laminated on a glass pane as rigid support.

retro-reflection (Fig. 2) [22,23]. Light from the illuminator is partially transmitted by the BS to the sample. The retro-reflected light is then partially reflected by the BS to the detector. With an ideal BS, that transmits 50% of the incident light and reflects the other 50% without any absorptive losses, the detected signal would be attenuated to $0.50 \times 0.50 = 0.25$. The method relies on prior knowledge of the exact optical properties of the BS, which depend on the direction as well as the wavelength of light.

1.4. Modelling retro-reflection

To predict the retro-reflective effect caused by geometric structures, computational techniques for the simulation of light propagation such as ray-tracing can be employed with detailed geometric models [24,25]. However, due to the model complexity and size resulting from such approaches if applied to extended CFS, methods hiding the optically complex internal mechanisms are often preferred. Functional descriptions of the BSDF allow to hide the geometric complexity of retro-reflective structures. Numerous analytical [26], numerical [27–29], and empirical [30] models for particular cases of retro-reflection have been proposed but are of no general applicability.

Data-driven models are of general applicability but rely on huge datasets. Basis functions such as wavelets or spherical harmonics provide a means to compress such datasets at resolutions adequate to replicate characteristic features of BSDFs [31–33]. RADIANCE as a validated lighting simulation software for visual comfort assessment [34] implements a data-driven model based on adaptive data-reduction applied to a discrete representation of the BSDF as a four-dimensional tensor [35,36]. The dimensions of the tensor relate to incident and outgoing direction via an equal-area mapping algorithm between square and disk [37,38]. An interface to measured data is provided, featuring an advanced interpolation algorithm to reconstruct the full BSDF from sparse measurements for few incident directions [39–41]. The model is capable to replicate the characteristics of a retro-reflective coating [14].

2. Materials and method

2.1. Exemplary sample of a retro-reflective coating

For the measurement of its BSDF, the retro-reflective coating was applied to a metal sheet of 150 mm × 150 mm. This sheet was subsequently laminated onto a flat glass pane. The glass as a rigid

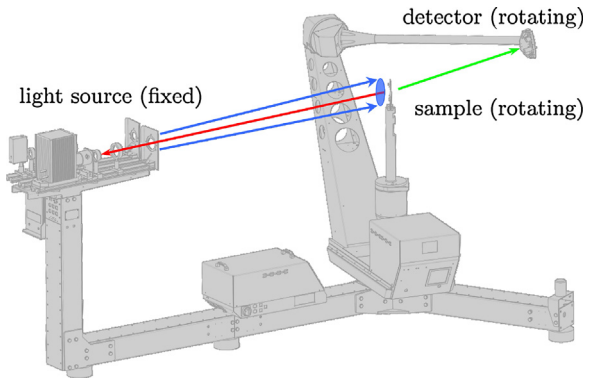

Fig. 4. Gonio-photometer employed in this study. The incident direction (red) is set by two-axis rotation of the sample. Rotation of the detectors on a spherical path around the sample continuously varies the outgoing direction (green) in the course of the measurement. Illustration based on imagery by pab advanced technologies Ltd, Freiburg. (For interpretation of the references to color in this legend, the reader is referred to the web version of the article.)

support prevents the sample from bending, which would affect the orientation of the measured surface region in the measurement. The sample is shown in Fig. 3. Surface imperfections are visible which are due to the prototype character of the specimen.

2.2. Measurement of the BSDF

A scanning gonio-photometer is chosen for the measurement for two reasons. First, since measurements are performed sequentially and independently at each pair of incident and outgoing directions, a higher dynamic range is achieved when compared to image-based techniques. The dynamic range is crucial to capture the expected, highly directional reflection by the sample as well as features of the BSDF where its value is low. Second, the open design of the instrument supports modifications.

The gonio-photometer in its default configuration is illustrated by Fig. 4. A light source with collimator is illuminating a spot on the sample from an invariant position. The size of this spot, which defines the sampling aperture over which the BSDF is averaged in the measurement, is adjusted to a diameter of ≈10 mm by slight focusing of the beam. The rotation of the sample over two axes defines the incident light direction. A detector mounted on a robotic arm is performing a continuous movement on a configurable path around the sample, varying the outgoing scattered light direction, and records irradiance at intervals of about 1 μs. The use of different semi-conductor devices such as silicon (Si) or indium gallium arsenide (InGaAS), optionally coupled with filters, allows to match a given spectral target response.

The BSDF of a sample is acquired by two subsequent measurements. First, the effective power of the light source on the sample P_i is determined by integration of the unobstructed beam's intensity distribution. Second, under identical illumination conditions, light scattered by a sample introduced into the beam is recorded by the detector as irradiance E at direction $(\theta_i, \phi_i, \theta_s, \phi_s)$. BSDF and differential scattering function (DSF) are calculated [19] as:

$$BSDF(\theta_i, \phi_i, \theta_s, \phi_s) = \frac{DSF(\theta_i, \phi_i, \theta_s, \phi_s)}{\cos\theta_s} = \frac{E_s(\theta_i, \phi_i, \theta_s, \phi_s)}{P_i \cdot \cos\theta_s} \quad (1)$$

2.3. Extension of the gonio-photometer to measure retro-reflection

To allow the measurement of the retro-reflected peak, the gonio-photometer is extended by two BSs as shown in Fig. 5.

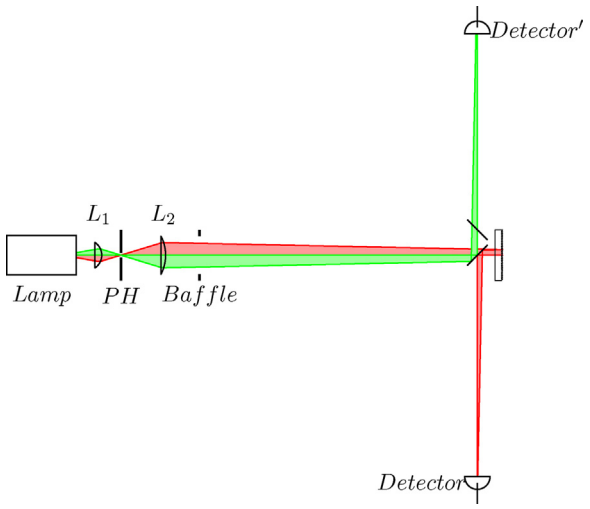

Fig. 5. Modified configuration for retro-reflection employing two BSs. *Detector′* (Green): reference measurement to characterize unobstructed beam. *Detector* (red): measurement of light scattered by sample. Light paths not contributing to the measurement, such as light reflected back to the source from the second BS, are not shown. (For interpretation of the references to color in this legend, the reader is referred to the web version of the article.)

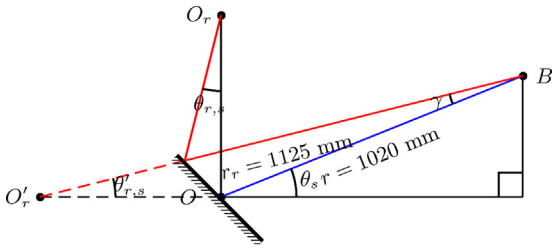

Fig. 6. The introduction of BSs extends the optical path from the centre of the sample at O_r to the detector at B. The scatter direction relative to the mirror image of O'_r is calculated from the direction relative to the centre of the detector rotation O.

The first BS is located at the center of rotation of the detector. The sample is pressed against a rigid mounting plate from the back. This plate is installed at a distance of 105 mm behind the beam-splitter and can be manually rotated around its vertical axis to set the incident elevation angle θ_i. As illustrated by the red beam, light is transmitted by the beam-splitter, is scattered by the sample back toward the incident direction, and then reflected from the BS to the detector at position *Detector*. This path is identical to the configuration in Fig. 2.

The chosen BS features equal transmission and reflection $\tau \approx 0.49$, $\rho \approx 0.49$ for the wavelength range of visible light 380–780 nm (Vis) and angle of incidence $\theta_{i,bs} = 45°$. However, to evaluate the shading performance of the coating, the entire solar spectrum including Vis and near infrared light 780 nm to 2500 nm (NIr) has to be accounted for. Transmission and reflection properties strongly depend on the wavelength and were e.g. measured as $\tau \approx 0.26$, $\rho \approx 0.72$ for NIr. An elaborate approach to account for this wavelength dependency would be to characterize the optical properties of the BS over the solar spectrum, and subsequently spectrally resolve the BSDF measurement. However, the high spectral resolution adds, in most cases of spectrally flat reflection unnecessary, complexity to the measurement and evaluation.

To compensate for the wavelength dependence of the BS's properties, a second, identical BS is placed next to the first at an angle of 90°. In analogy to the beam characterization in the BSDF measurements employing the gonio-photometer's default configuration, the unobstructed beam is measured at position *Detector′* via one reflection on the first, and one transmission by the second BS (green

beam in Fig. 5). Since both light paths (green and red) involve one reflection and one transmission event on identical BSs, exact a priori knowledge of their properties, which vary for different wavelength ranges, is not required. This assumes that that the sample's reflection spectrum is flat within the wavelength range covered by one measurement and greatly simplifies the measurement.

Due to the location of the sample behind the detector's center of rotation, its optical distance to the detector (r_r, red in Fig. 6) does not match the detector radius (r, blue in Fig. 6). The effective scatter direction $\theta_{r,s}$ according to the extended optical distance r_r can be found from the direction relative to the centre of the detector radius θ_s as recorded by the instrument:

$$\sin\theta_{r,s} = \frac{r}{r_r} \cdot \sin\theta_s \tag{2}$$

The measured datasets resulting from the measurement are rotated so that the angular offset of 90° caused by the BSs is compensated, and all data exceeding ±7.5° from the direction of ideal retro-reflection is culled. The resulting BSDF, limited to the region of the peak that cannot be otherwise measured, is finally combined with a measurement on the unmodified gonio-photometer excluding the peak region.

2.4. Testing of the extended gonio-photometer

To test the method, the BSDFs of a front-side mirror as measured with and without BSs are compared.

For retro-reflection occurring at normal incidence ($\theta_i = 0°$, $\phi_i = 0°$), a direct comparison with the gonio-photometer's default configuration is not possible due to the shading of the light source by the detector. Instead, the BSDF at scattered directions close to the peak region that can be measured with the default configuration and with the extended setup are compared. Any discontinuity of the BSDFs acquired by the two different setups is considered an artifact introduced by the method.

An important source of error in the peak region, characterized by a steep gradient, is misalignment of the sample in the measurements with and without beam-splitters. Alignment errors are expected to a certain degree due to the experimental nature of the instrument extension. To correct for this expected misalignment, the dataset resulting from the measurement employing BSs is rotated so that the maximum BSDF is located at $\theta = 0°$.

A second measurement for one incident direction ($\theta_i = 10°$, $\phi_i = 0°$), employing only the default configuration, shall allow to test the capability of the method to capture details in the BSDF at high directional resolution. The peak shape for adjacent incident directions is expected to change only gradually. A strong disagreement of the peak shape with the measurement employing BSs at ($\theta_i = 0°$, $\phi_i = 0°$) would therefore indicate an error in the method.

2.5. Measurement of the sample's BSDF

The characterization of the retro-reflective sample assumes isotropy and is performed for one invariant in-plane angle $\phi_i = 0°$ in NIr and Vis. The incident elevation angle (angle between the surface normal and the light source direction) is set to $\theta_i = 5°$ and $\theta_i = 10–70°$ in steps of 10°. Incident elevation angles above 70° are affected by shadowing due to the thickness of the plate holding the sample, and therefore not included in the measurement.

First, the BSDF of the entire reflection hemisphere (outgoing $\theta_s = 0–90°$, $\phi_s = 0–360°$) is scanned by the gonio-photometer in its default configuration. Directions close to retro-reflection, which are affected by the occlusion of the light source, are filtered from the datasets.

Second, the extended configuration with two BSs is employed to scan only the region of the retro-reflective peak (incident light direction ±7.5°). Since the outgoing directions are effectively mirrored over the first BS (Fig. 5), post-processing has to transform the coordinates of the acquired data-points to match the coordinate system of the gonio-photometer in its default configuration. The measurement of the unobstructed peak is rotated from ($\theta_s = 90°$, $\phi_s = 180°$) to ($\theta_s = 180°$, $\phi_s = 0°$) and P_i is computed by integration. Distributions of light scattered by the retro-reflective sample are rotated from ($\theta_s = 90°$, $\phi_s = 0°$) to ($\theta_s = 0°$, $\phi_s = 0°$). In a final transformation step, the rotation is adjusted so that the maximum recorded value is located at the ideal direction of retro-reflection, and the BSDF is computed applying Eq. (1).

Data-points of the hemispherical scan and of the peak region are merged into one data-set per incident direction, covering the entire reflection hemisphere including the retro-reflected peak region.

Plots of the DSF in the scatter plane, defined as containing the incident direction (θ_i, ϕ_i) and the surface normal of the sample, illustrate the measured distributions. A logarithmic scale ensures visibility of the background scatter in distributions featuring strong peaks as expected for both the mirror and the retro-reflective sample.

2.6. Generation of a data-driven model from the measured BSDF

For each measured incident direction and wavelength range, the RADIANCE command `pabopto2bsdf` generates a set of Gaussian basis functions approximating the BSDF over all outgoing directions. Between adjacent incident directions, a mass transport algorithm is employed by `bsdf2ttree` to interpolate and generate a discrete representation of the BSDF at chosen resolution. In the general case of anisotropic reflection, this results in a tensor of four dimensions relating to θ_i, ϕ_i and θ_s, ϕ_s. However in the case of isotropy, with invariant ϕ_i in the measurement, the BSDF can be stored in a data cube of three dimensions. The resolution is parametrized as a power of 2 for each dimension, so that a resolution parameter k leads to $2^{4 \cdot k}$ elements in the general case of anisotropy, or $2^{3 \cdot k}$ for isotropy. In an optional, final pass, adjacent elements of the tensor with low variance are joined until a data-reduction target is met given. The resulting hierarchical representation as a compact, multi-dimensional tree structure is embedded into a XML format that can be loaded into RADIANCE and applied to any geometric primitive via the `BSDF` material type.

The method is applied to the measured BSDFs of the retro-reflective sample to generate a data-driven model of high directional resolution for each wavelength range. The measured datasets for NIr and Vis, each corresponding to one incident direction, are compiled into interpolants:

```
pabopto2bsdf  05.dat  10.dat  20.dat
30.dat  40.dat  50.dat
60.dat  70.dat >sample.sir
```

The resolution parameter k is set to 7, leading to a data-cube of $2^{3 \cdot 7} = 2{,}097{,}152$ elements. The subsequent data-reduction pass with a reduction target of 95% reduces the data-set to a compact model of ≈104,858 elements:

```
bsdf2ttree  -t3  -g 7  -t 95
sample.sir >sample.xml
```

The resulting XML file can be loaded by RADIANCE to define a material that can be assigned to any geometrical entity:

```
void  BSDF  retroreflectiveMat
6  0  sample.xml  0  1  0.
0
0
```

This defines a material description `retroreflectiveMat` referring to the data-driven model embedded in `sample.xml` as generated from the measurements. The second line of above example sets a zero thickness (second numerical value) and relates the

Table 1
Reflection properties of the slats in the comparison of the retro-reflective with ideally diffuse and specular coatings.

	Case *A*	Case *B*	Case *C*
Top	Retro-reflective	Specular $\rho = 0.8$	Diffuse $\rho = 0.8$
Bottom	Diffuse $\rho = 0.8$	Diffuse $\rho = 0.8$	Diffuse $\rho = 0.8$

in-plane reference, which is of no relevance for the case of isotropic reflection, toward the positive *y*-axis.

2.7. Modeling the effect of retro-reflection in Venetian blinds

To assess the effect of the retro-reflective coating, it is compared to ideally diffuse and mirror-like slats of a Venetian blinds assembly embedded in a triple-glazing unit. The slats are flat and tilted horizontally. The depth and the vertical distance of the slats are equally set to 10 mm. Under the given sky condition, this prevents direct transmission of sunlight and thereby allows the evaluation of the effect of the reflection properties of the blinds.

Perfectly flat slats are far from realistic components of Venetian blinds. Market-available CFSs comprise slats featuring geometries that are highly optimized for visual comfort and control of solar gains. However, reducing the geometry of the slats to planar surfaces allows the isolated inspection of effects caused by the reflection properties in a shading device causing minimum view obstruction.

The retro-reflective coating is applied to the upper surface of the slats in case *A* with the bottom sides being ideally diffuse. The slats comprising case *B* feature a mirror-like top and ideally diffuse reflection on the bottom surface. In case *C*, both surfaces share the perfect diffuse reflection properties.

The blinds are embedded in a glazing assembly comprising an uncoated glass pane toward the exterior, and two coated glass panes toward the interior.

An overview of the reflection properties of the slats is given in Table 1.

The ideally diffuse and specular reflection properties of the blinds and glazing are modeled by the built-in material models in RADIANCE:

```
void metal mirrorMat
0
0
5                .8                .8                .8
                 .9                0

void plastic diffuseMat
0
0
5                .8                .8                .8
                 0                 0

void glass exteriorMat
0
0
3                .99               .99               .99

void glass interiorMat
0
0
3                .775              .775              .775
```

For the assessment of daylight performance in Vis, photometric data-driven models of the blinds assemblies for all three cases, including the glazing, are generated using `genBSDF`. `genBSDF` is a ray-tracer for the computation of BSDFs from geometric models and distributed as part of RADIANCE. In analogy to the data-driven model of the retro-reflective coating, the BSDF of the fenestration system is a full description of the light scattering properties of blinds assembly and glazing. Other than the isotropic reflection model of the coating, the data-driven models of the fenestration replicate anisotropic transmission as well as reflection from front and back.

Table 2
Parameters in the generation of the BSDFs of Venetian blinds and glazing with `genBSDF`.

Parameter	Description	All cases	Case *A*
-t4 *k*	Tensor resolution exponent, results in $2^{4 \cdot k}$ coefficients	6	
-c *n*	Sample rays per hemisphere	32,768	
-ad *n*	Number of daughter rays at each ambient ray intersection	128	
-lw *w*	Maximum weight of single ray contribution	0.008	
-ss *n*	Number of specular samples		128

Table 3
Solar-optical properties (visible, solar transmission τ_{vis}, τ_{sol} and front, back emissivity ϵ_f, ϵ_b) as provided by the International Glazing Database (IGDB) for glazings of given ID.

Description	Variant	ID	τ_{vis}	τ_{sol}	ϵ_f	ϵ_b
Outer, uncoated pane	*both*	14,706	0.912	0.905	0.840	0.840
Inner, coated panes	L_eL_τ	4407	0.858	0.522	0.053	0.841
	L_eH_τ	21457	0.887	0.715	0.086	0.840

Parameters set in the generation of the fenestration BSDFs at high resolution in Vis are listed in Table 2. Prior to data-reduction, the tensors for all three fenestration BSDFs comprise $2^{4 \cdot k} = 16{,}777{,}216$ elements for of the four BSDF components describing front and back reflection and transmission. This corresponds to 4096 incident and 4096 outgoing scattered directions for each component. The -c parameter, set to 32,768, determines the number of sampled rays for each incident direction. This ensures that, as an average, 32.768/4096 = 8 rays are sent for each pair of incident and outgoing directions to random locations on the non-uniform surface of the fenestration system. The -ad and -lw parameters control the sampling on diffuse surfaces. Only for case *A*, an additional parameter -ss causes the generation of 128 rays at each specular reflection to sufficiently cover the width of the peak region as described by the data-driven reflection model.

A second set of BSDFs, both in Vis and NIr, is generated from the measurements of the coatings, and identical reflection values for Vis and NIr for all other surfaces. These BSDFs represent only the blinds assembly without glass layers. They are generated employing a fixed directional basis of 145 incident and 145 outgoing directions. The resulting BSDFs for each case are merged into one XML file, which consequently holds a description of light scattering in the entire solar spectrum.

For each case, the solar BSDF of the blinds assembly is combined with descriptions of the glazing layers in WINDOW [42]. The blinds are embedded in a glazing assembly comprising an uncoated pane to the outside, and two coated panes with 90% Argon fill to the inside. Two variants of the coated panes are prepared for each case.

The first variant, L_eL_τ, comprises panes of low emissivity and low solar transmission. Its properties in Vis correspond to the glazing description in the daylight performance evaluation.

Variant L_eH_τ combines low emissivity with high solar transmission. Selected optical properties of the glass layers, as provided by the International Glazing Database (IGDB) from within WINDOW, are listed in Table 3.

For each of the three cases and both variants, the solar heat gain coefficient (SHGC) and direct-hemispherical solar transmission $\tau_{d,sol}$ are computed in WINDOW to assess the shading performance

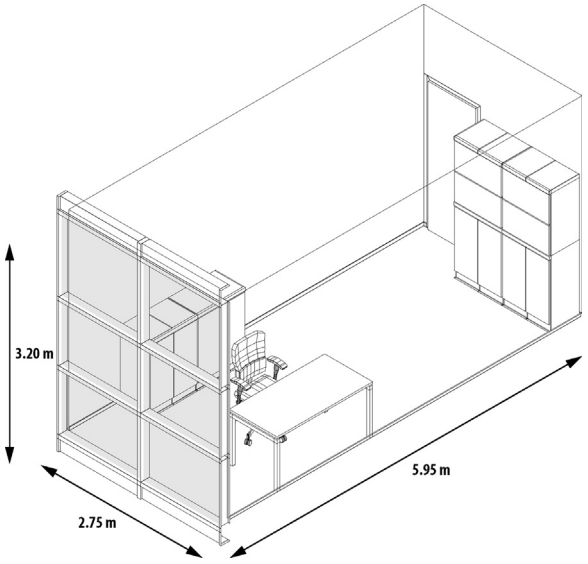

Fig. 7. Cellular office [38] as a test case for the comparison of the retro-reflective coating with ideally diffuse and specular slats. The lowest zone of the fenestration is opaque.

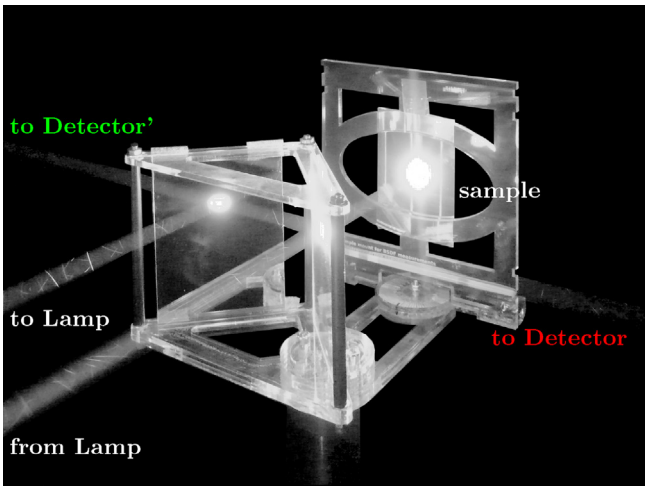

Fig. 8. Prototype implementing the design outlined in Fig. 5. Light reflected back to the lamp is discarded.

and, with variant L_eH_τ, the potential to make controlled use of solar gains.

While $\tau_{d,sol}$ is a purely optical property describing the transmission of radiation at short wavelengths, SHGC comprises of $\tau_{d,sol}$ and the inward flowing fraction of radiation emitted by the fenestration layers. Both SHGC and $\tau_{d,sol}$ are calculated for one incident elevation angle $\theta = 50^\circ$, when the blinds fully occlude direct sunlight and transmission through the assembly is limited to reflection on the slats.

2.8. Testing the model in an exemplary test room

The effective daylight performance of the three glazing systems is tested for an exemplary cellular, South-oriented office (Fig. 7). The office is directly exposed the sun in the South at an elevation of 50°. This sky condition agrees with the exemplary case chosen for the calculation of SHGC and $\tau_{d,sol}$, and ensures that direct sunlight is entirely occluded geometrically by the chosen horizontal orientation of the blinds. These idealized sky conditions are chosen to illustrate the coating's effect in a comprehensive manner. An evaluation aiming at representative results would have to consider manual or automated control of the blinds, and asks for climate-based daylight modeling (CBDM) techniques and annual metrics.

The BSDFs in Vis representing the glazing systems of the three cases *A*, *B* and *C* are employed to invisible surfaces enclosing the fenestration geometry in the model. These BSDFs are queried only when the enclosing surfaces are hit by rays as part of the stochastic, indirect-diffuse calculation module of RADIANCE, geometrical ray-tracing within the fenestration does not take place. This use of the BSDF as a "black box" in the indirect-diffuse calculation simplifies the simulation, since complex light propagation within the fenestration is computed only once in the generation of the data-driven model. Furthermore, the data-driven model overcomes a limitation of the backward ray-tracing algorithm in the treatment of specular, redirecting systems, which would otherwise require techniques such as the introduction of virtual light sources or forward-tracing extensions [43].

In the direct, deterministic calculation module of RADIANCE, rays pass the enclosing surfaces unaffected and take part of a full ray-tracing calculation through the fenestration system. This preserves visibility of the geometric detail, such as the slats, and pronounces shadow patterns due to direct sunlight.

For all cases *A*–*C*, illuminance on the interior surfaces of the office, as seen by an occupant facing the fenestration, and horizon-

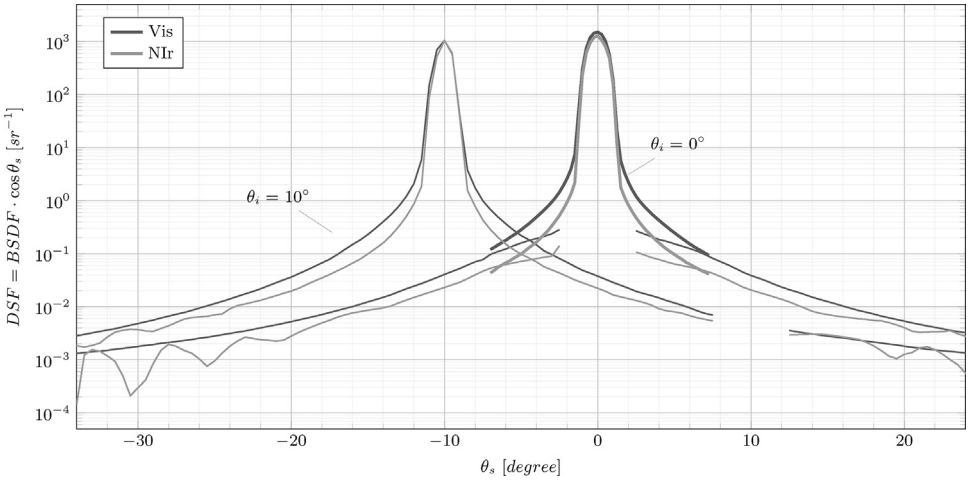

Fig. 9. Profile of the mirror's DSF in the scatter plane, Vis and NIr. The peak-region measured through the BSs is indicated by an enhanced line-width.

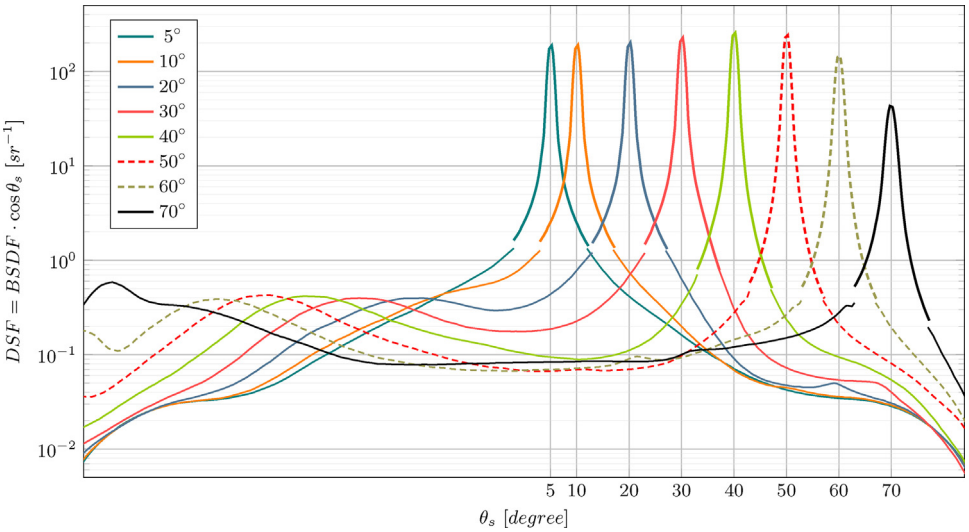

Fig. 10. Profile of the retro-reflective sample's DSF in the scatter plane measured in the wavelength range of Vis.

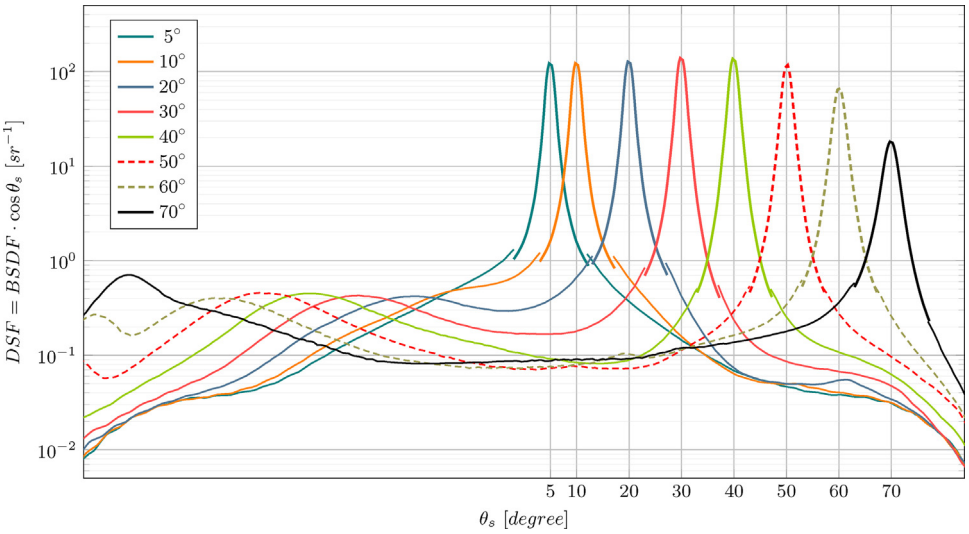

Fig. 11. Profile of the retro-reflective sample's DSF in the scatter plane measured in the wavelength range of NIr.

tal illuminance on the working plane are computed as a measure of shading by the flat blinds under ideal conditions for view-through.

For identical viewing conditions, luminance maps are generated. Other than the illuminance distribution, the luminance maps also reflect the reflection properties of the interior surfaces.

The glare evaluation software EVALGLARE is employed to compute Daylight Glare Probability (DGP) and Daylight Glare Index (DGI) as metrics for the evaluation of discomfort glare by daylight from the luminance maps [44,45]. The two metrics differ in that the formulation for DGP considers the vertical illuminance E_v reaching the eye of an observer as potential cause of discomfort glare, as well as to account for adaption effects which is accounted to background luminance L_b in the formulation of DGI.

3. Results and discussion

3.1. Extension of the gonio-photometer

A prototype of the setup as illustrated in Fig. 5 is shown in Fig. 8. It comprises laser-cut acrylic parts holding two beam-splitters. The acrylic parts are held by PVC tubes and threaded rods. An additional baffle is attached to the mounting plate during measurements to prevent direct light scattering from the sample to the detector. The prototype replaces the sample mount of the default configuration. Since the beam-splitters orientation toward the light source must be kept fixed, the incident elevation angle θ_i is manually set by rotation of the mounting plate.

3.2. Testing of the measurement method

Fig. 9 shows the DSFs of the mirror close to the specular peak, as measured in the wavelength ranges of Vis and NIr for two incident directions. The data-set for $\theta_i = 0°$ comprises measurements with and without BSs. For $\theta_i = 10°$, no BSs were employed and therefore no reflection data is present in the region around the incident direction.

For DSF values above 10, the widths of the peaks in both wavelength ranges match. The peak is wider in the range of Vis than NIr for values below 10. For values lower than 0.01, low frequency noise in NIr is apparent, which can be explained by a known drift mostly due to temperature effects at low signal levels. This effect does not occur in the range of Vis. These observations equally apply to the measurements with ($\theta_i = 0°$) and without BSs ($\theta_i = 10°$).

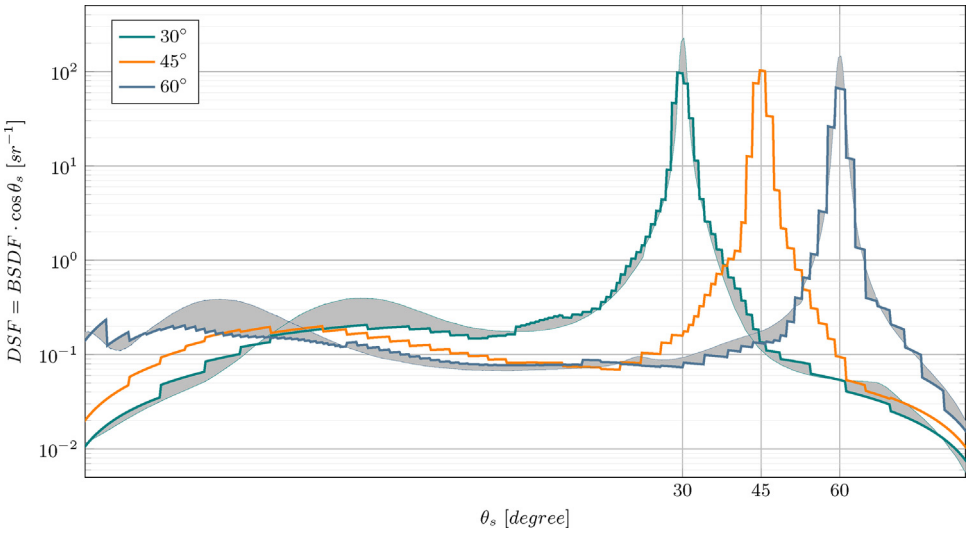

Fig. 12. Profile of the retro-reflective sample's DSF in the scatter plane as returned by the data-driven model in the wavelength range of Vis. The deviations from measurements for $\theta_i = 30^\circ$ and 60° are shaded.

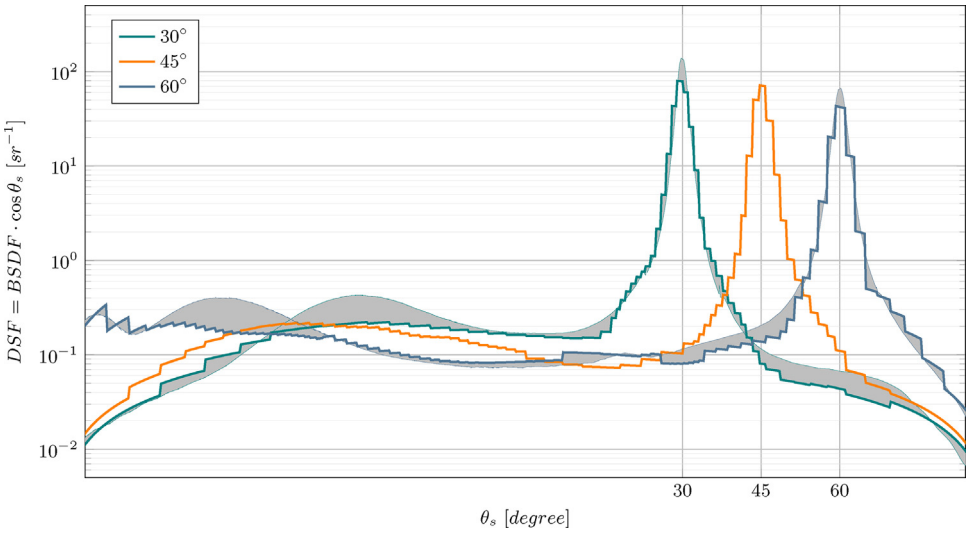

Fig. 13. Profile of the retro-reflective sample's DSF in the scatter plane as returned by the data-driven model in the wavelength range of NIr. The deviations from measurements for $\theta_i = 30^\circ$ and 60° are shaded.

The measurement for $\theta_i = 0^\circ$ without BSs shows artifacts caused by shading in the ranges $\theta_s = -7.5 - -2.5^\circ$ and $\theta_s = 2.5 - 7.5^\circ$. Datapoints in this region are typically excluded and only shown here to illustrate the effect. The distributions for $\theta_i = 0^\circ$ show a minor discontinuity at the joint datasets for the hemisphere and the peak region at negative θ in both wavelength ranges. The distributions agree at positive θ.

The overall accordance between the measurements confirms the validity and the in-principal applicability of the method to the problem. The method is applicable for surfaces featuring strong peaks, leading to high signals in the entire peak region. This is the case for the sample that is to be evaluated in this study, and motivated the development of the instrument extension specifically for the peak region.

3.3. Measured BSDF of the coating

The DSFs of the sample, measured at eight incident directions in the wavelength ranges of Vis and NIr, are presented in Figs. 10 and 11.

The coating exhibits a strong directional peak toward the incident direction in both wavelength ranges. The heights of the peaks are approximately equal for incident directions in the range of $\theta_i = 5 - 50^\circ$, and then moderately decrease toward the highest measured $\theta_i = 70^\circ$.

Lower, wide lobes are present in the forward direction. However, the magnitude of the retro-reflected peaks is about two orders of magnitude higher than the forward lobes.

Compared to the front-side mirror, a distinct diffuse background is visible but about three orders of magnitude lower than the peaks. The presence of this background can be confirmed visually since the sample does appear in a bright gray under directional illumination.

A discontinuity exists between the hemispherical measurements and the DSF of the peak region, which is measured employing the two BSs. In Vis, the peak is positively offset compared to the background, while a negative offset occurs in NIr.

Alignment errors can be excluded to cause this effect, since measurements in both wavelength ranges are conducted without change to the geometric setup.

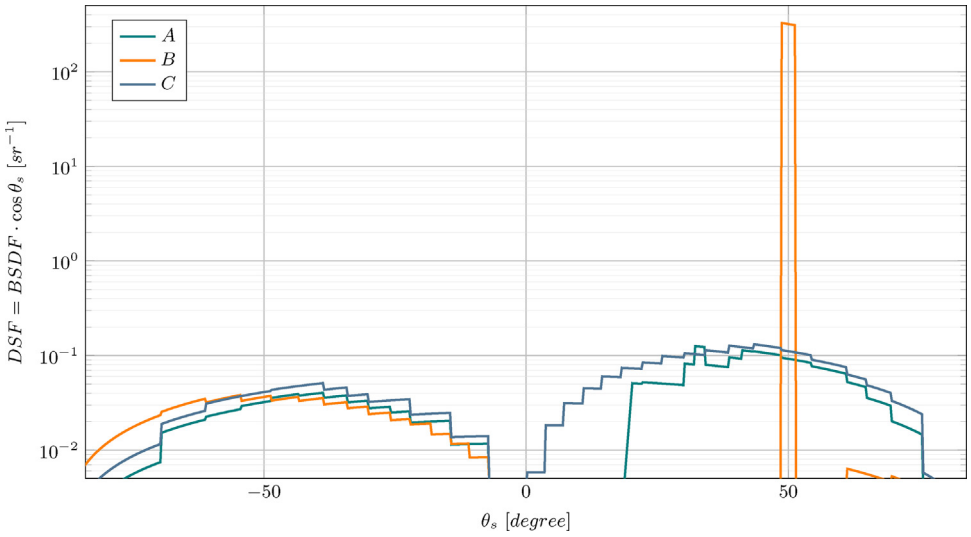

Fig. 14. Profile of the fenestration system DSFs in the scatter plane for transmission in Vis. Coordinates are relative to the fenestration plane. $\theta = 0°$ points inward, positive θ upward.

Table 4
Comparison of the data-driven model with the measured DSF of the retro-reflective coating in the scatter plane by frequency of deviations ΔDSF and coefficient of variation of the root-mean-square deviation $CV(RMSD)$.

	θ_i	$CV(RMSD)$	ΔDSF< 5%	ΔDSF<10%	ΔDSF<20%
Vis	30°	4.041	7.8%	14.4%	36.3%
	60°	3.713	4.4%	11.9%	50.1%
NIr	30°	2.677	9.7%	25.2%	41.9%
	60°	1.900	11.6%	25.5%	52.9%

Table 5
Direct-hemispherical reflection integrals derived from model ($\rho_{dh,mod}$) and measured DSF ($\rho_{dh,mea}$) of the retro-reflective coating.

	θ_i	$\rho_{dh,mea}$	$\rho_{dh,mod}$	$\Delta\rho_{dh}$
Vis	30°	0.813	0.815	0.3%
	60°	0.663	0.656	−1.1%
NIr	30°	0.750	0.732	−2.4%
	60°	0.646	0.631	−2.3%

One possible cause for the discontinuities are thermal effects at the detectors in particular when the measured signal is low. The gonio-photometer is operated in an environment with a temperature set to ≈20 °C, but no direct cooling of the detectors. Thermal noise is compensated by subtraction of a fixed offset value from the signal. This offset is determined under stabilized thermal conditions. Setting of incident directions, when employing the BSs, is done manually by a person accessing the laboratory from the outside, and affects the temperature in the laboratory. Since the BSs decrease the overall signal range, the impact of thermal effects is high. On the other hand, for measurements of the reflection hemisphere excluding the peak, the incident direction is set automatically without manual intervention. The temperature in the lab thus remains stable and, furthermore, the impact of thermal effects is lower due to higher measured signals.

The role of thermal effects will be further investigated but, since they affect only the lower region of the peak measurements, are expected to have little effect on the validity of the results.

3.4. Data-driven reflection model from measured BSDF

The profiles of the DSF in the scatter plane, as predicted by the data-driven model for three exemplary incident directions $\theta_i = 30°$, 45° and 60°, are shown in Fig. 12 (Vis) and Fig. 13 (NIr). For two incident directions $\theta_i = 30°$, 60° the corresponding measurement data is underlaid. The distributions for $\theta_i = 45°$ are the result of interpolation. In analogy to the measured DSF, the models show high accordance in both wavelength ranges.

The shapes of the retro-reflected peaks are closely matched by the models for both measured directions. They also seam to be plausible for the third direction, where no direct comparison to measurements is possible. The discrete nature of the data-driven model, even at high directional resolution (≈1.5°), results in a flattened peaks. The locally adaptive resolution is high in the peak region and closely matches the shape over several decades.

The forward lobes of the distributions are present in the model output, but appear less pronounced and do not match the measurement as closely as the peaks. The interpolation algorithm seams to strongly favor peak regions when fitting the measured distributions. Note that the amplitude of the forward peak is low and pronounced in the plots by the logarithmic scale.

Step artifacts introduced by the local data-reduction are apparent at lower values of the DSF. However, due to the broadness of the forward peak, the reduced directional resolution in these regions does not lead to a stronger mismatch with the measurement. The locally adaptive data-reduction appears to be well suited to maintain the sample's highly directional reflection characteristics, with most reflected power concentrated in a narrow peak region and a wide range of directions of little variance.

While the qualitative evaluation confirms the presence of all important features of the measurement in the data-driven model, a quantitative comparison reveals high local deviations. About half of the values in the scatter plane deviate more than 20% from the measurement. This is expected since the discrete model effectively distributes the power contained in the peak over an extended solid angle, and replaces less pronounced features by coarse approximations due to the adaptive data-reduction. The limited peak resolution in particular may affect visual comfort assessments if focused highlights occur in the field of view. In the case of retro-reflection, this effect seams to be not critical, since specular reflection of sunlight is directed to the outside.

In terms of direct-hemispherical integrals, the data-driven model achieves a high degree of accordance as shown in Tables 4 and 5 for two incident directions.

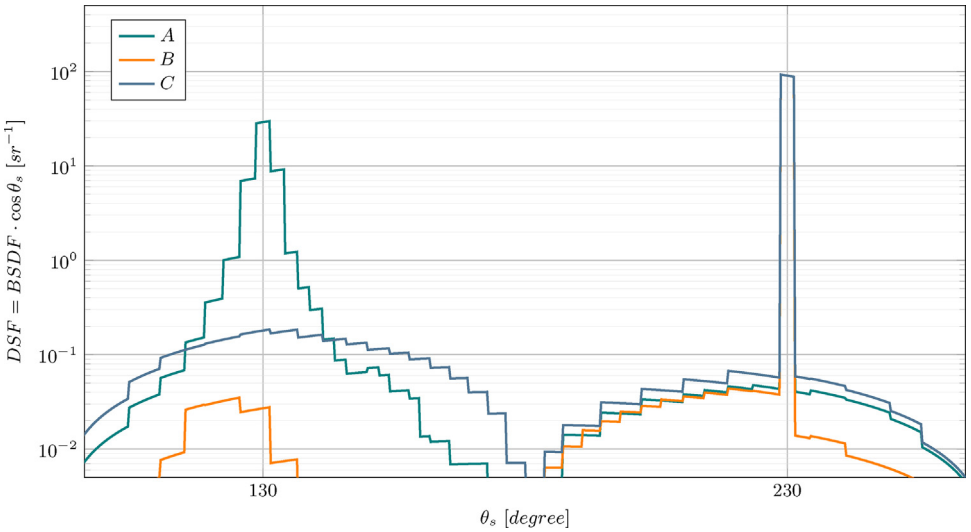

Fig. 15. Profile of the fenestration system DSFs in the scatter plane for reflection in Vis. $\theta = 180°$ points outward. θ =90–180° is above, θ =180–270° below the horizon.

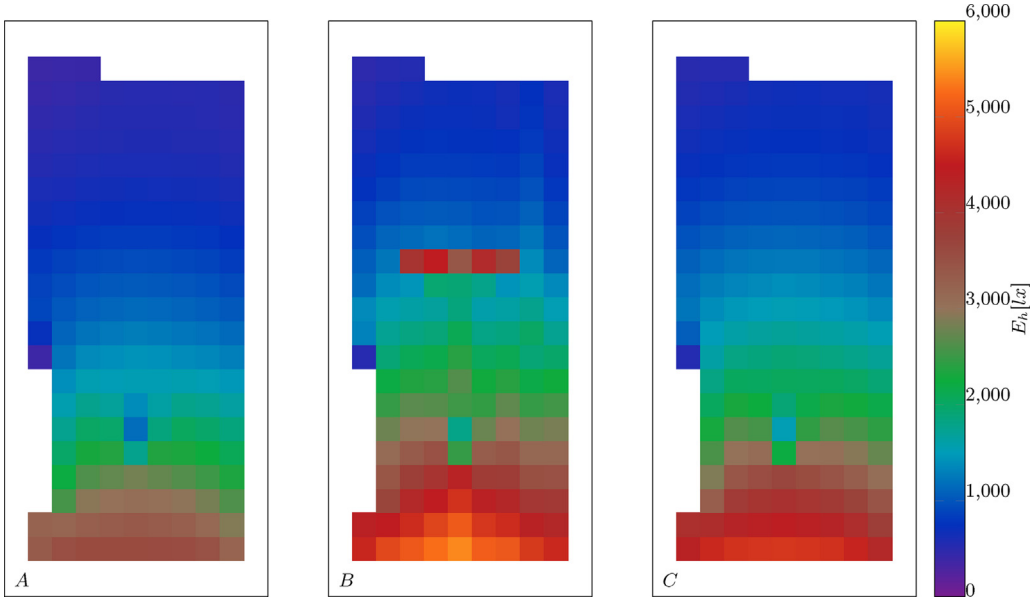

Fig. 16. Distribution of horizontal illuminance on a sensor grid at $z = 0.85$ m (bottom = South). Black frames indicate the room's outlines. Under the assessed conditions, all cases achieve $E_h > 300$ lx unless covered by furniture (left column, top row).

Table 6
Solar gains glazing variant L_eL_τ, cases *A*–*C* for exemplary sun elevations (values for the evaluated sun elevation 50° in bold letters).

	40°		50°		60°	
	SHGC	$\tau_{d,sol}$	SHGC	$\tau_{d,sol}$	SHGC	$\tau_{d,sol}$
A	.2279	.1024	**.1526**	**.0520**	.1390	.0466
B	.4484	.2602	**.3947**	**.2030**	.2677	.1058
C	.2838	.1356	**.2241**	**.0925**	.1996	.0817

3.5. *Effects of retro-reflection in Venetian blinds*

Figs. 14 and 15 show the photometric DSF for the fenestration systems, including glazing, in the scatter plane and for one incident elevation $\theta_i = 130°$. Angular coordinates are relative to the fenestration plane, with $\theta = 0°$ corresponding to the inside. The shown distributions therefore correspond to a sun elevation of 50°.

Light transmitted through the system by upward reflection on the mirror blinds (case *B*) to $\theta_s = 50°$ is the most prominent feature in the transmission distributions. While all systems feature diffuse transmission downward due to identical reflection properties of the bottom surfaces of the slats, only for cases *A* and *C* a diffuse upward transmission occurs.

All systems show a pronounced peak at $\theta_s = 230°$ due to reflection on the outer glass surface, and diffuse downward reflection by the bottom surfaces of the slats. Retro-reflection causes a peak toward the incident direction for case *A*.

While light scattering by case *A* is characterized by the retro-reflection to the outside, and case *B* by the almost exclusive, directional transmission to the inside. Since the blinds assembly of case *C* scatters light equally to the inside and outside, the DSFs for transmission and reflection differ only due to the different transmission of the inner and outer glazing.

The solar gains for both glazing variants and all three cases as predicted by WINDOW are listed in Tables 6 and 7. The sun elevation angle of 50° reflects the condition for which the blinds inclination angle is set and are evaluated. The values for 40° and 60° indicate the sensitivity to the incident direction.

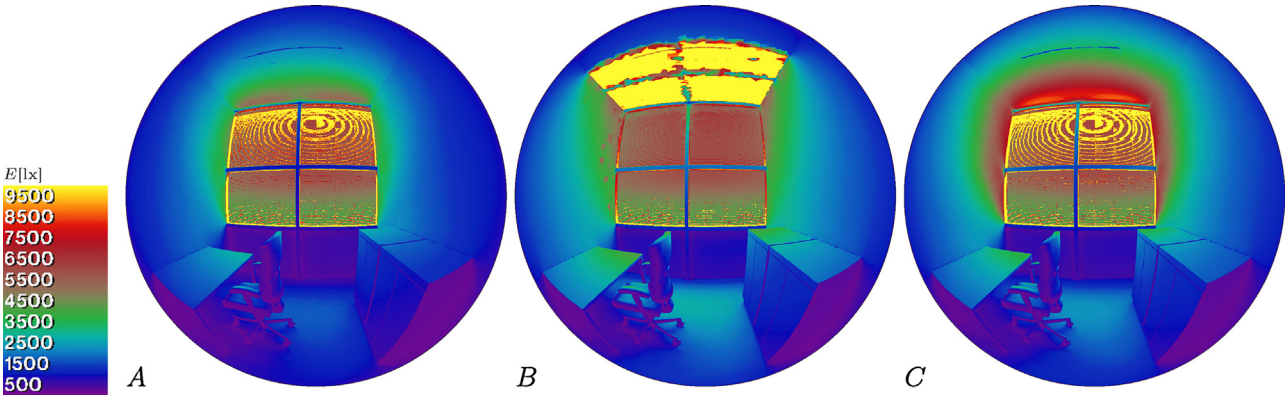

Fig. 17. Distribution of illuminance E [lx] on the surfaces of an exemplary, South-facing office with flat blinds featuring retro-reflective (case *A*), ideally mirror-like (*B*), and ideally diffuse (*C*) top surfaces. Sun elevation 50°, azimuth 0° (South).

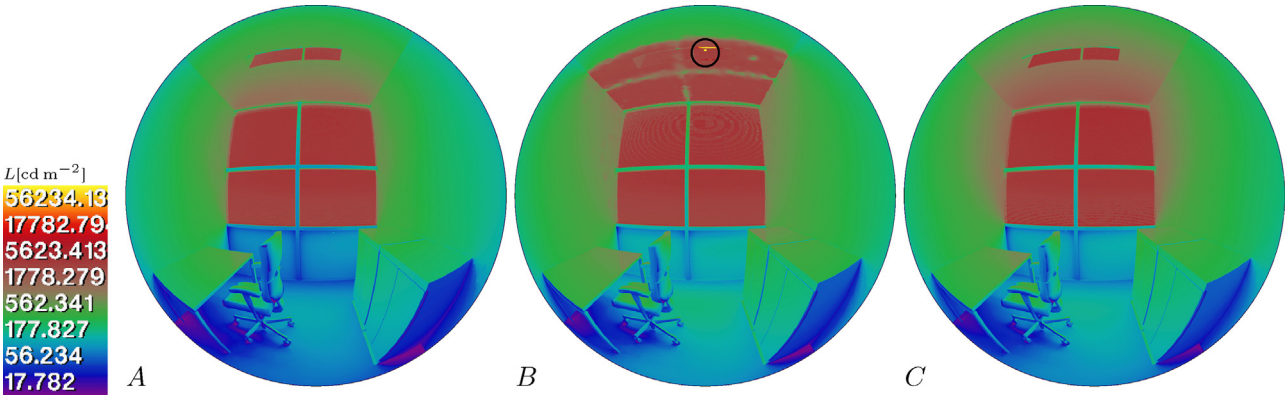

Fig. 18. Luminance maps [cd m^{-2}] for cases *A*, *B* and *C*. Note the reflection of the sun in the luminaire in case *B* marked by the black circle.

Table 7
Solar gains glazing variant L_eH_τ.

	40°		50°		60°	
	SHGC	$\tau_{d,sol}$	**SHGC**	$\tau_{d,sol}$	**SHGC**	$\tau_{d,sol}$
A	.2803	.1680	**.1823**	**.0873**	.1653	.0778
B	.5752	.4197	**.4978**	**.3382**	.3279	.1841
C	.3540	.2254	**.2746**	**.1559**	.2441	.1366

For both glazing variants, solar gains are highest if the mirror-like top surfaces reflect direct sunlight to the interior (case *B*).

Slats with diffuse reflection on top and bottom surfaces (case *C*) lead to a decrease of shortwave transmission by ≈50% when compared to the mirror blinds (case *B*). The decrease of SHGC by ≈45% is less pronounced due to increased longwave emission by the blinds.

The retro-reflective coating (case *A*) achieves the lowest solar transmission and SHGC. Compared to case *B*, solar transmission is reduced by ≈75% and SHGC by ≈60%. The coating combines minimal forward transmission due to its retro-reflective property, and low emission due to the high directionality of retro-reflection. It minimizes diffuse inter-reflection and thereby absorption within the blinds assembly, effectively limiting the emission toward the interior.

3.6. Effects on daylight admission and distribution

The different reflection properties of cases *A*–*C* effect the shading and thereby the daylight supply in the attached office space. The illuminance distributions calculated on a 0.25 m by 0.25 m sensor grid at 0.85 m height are show in Fig. 16. Under the assessed sky condition and configuration of the blinds geometry, all three cases maintain a high horizontal illuminance of $E_h > 300$ lx. Extremely high values for E_h occur close to the fenestration in cases *B*, *C*. These are avoided by the retro-reflective coating *A*, leading to an even illuminance distribution. Specular reflection of the incident sunlight by the blinds' top, and the luminaire's downward surfaces, lead to locally high E_h at a distance of ≈4.00 m from the fenestration.

The illuminance distributions for the three cases are presented with a linear color-mapping in Fig. 17. Due to the geometrical configuration of the blinds, sunlight for the given elevation angle of 50° is not directly transmitted through the window.

The retro-reflective coating as in case *A* achieves an effective shading by suppressing reflection to the interior. Illuminance is in the range of 500–2000 lx on all opaque surfaces but the side-walls and ceiling. On the walls in direct proximity to the window, a weak effect of diffuse skylight and scattering of sunlight by the slats is apparent and results in a higher illuminance of up to ≈4000 lx. Forward reflection causes a high illuminance on the ceiling close to the window up to ≈5500 lx.

The mirror-like reflection of light from the slats comprising the blinds assembly in case *B* produces a projection of the window aperture to the ceiling. Consequently, illuminance reaches up to ≈20,000 lx on the ceiling. Illuminance on the other opaque surfaces, illuminated mostly by light reflected from the ceiling ($\rho = 0.8$), is in the range of 500–4000 lx and up to ≈5000 lx on the side-walls adjacent to the window.

When compared to case *B*, the diffuse reflection by the slats in case *C* results in less extreme maximum illuminance of ≈8000 lx, which is limited to the ceiling in immediate proximity of the window. However, the illuminance on the opaque surfaces is consistently higher than in case *A*.

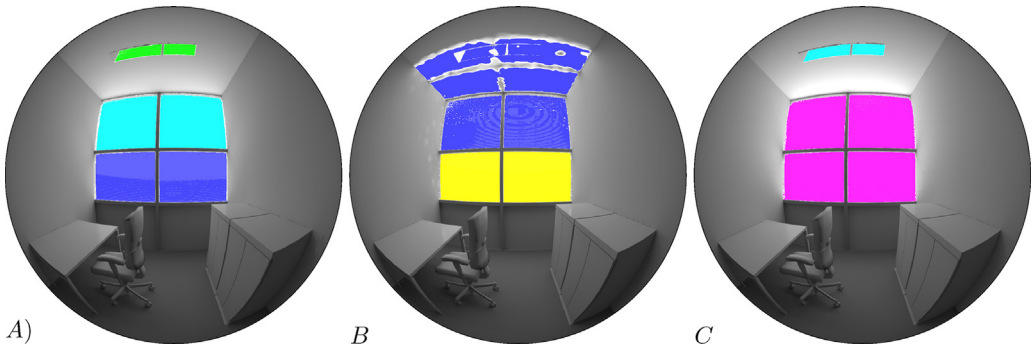

Fig. 19. Potential glare sources for cases *A*, *B* and *C*.

Table 8
Results of glare assessments for the three cases of retro-reflective (*A*), specular (*B*), and diffuse (case *C*) blinds.

	Case *A*	Case *B*	Case *C*
DGP	0.328	0.888	0.352
DGI	23.931	29.340	22.310
E_v [lx]	2235.396	8604.529	2712.936
L_b [cd m^{-2}]	211.629	256.865	313.257

Fig. 18 shows the luminance maps for the three cases. A logarithmic color map is applied to cover the dynamic range of the imagery. As can be expected, the luminance on the diffuse surfaces is in accordance with the illuminance distributions in Fig. 17. The specular reflection on the luminaire's surface at the ceiling produces a mirror image of the fenestration, and therefore high luminance values in all three cases. The highest pixel values are present in case *B*, where the reflected sun-disk is visible on the luminaire with a maximum luminance of ≈850,000 cd m^{-2}.

The glare assessment of the three cases considers not only the opaque surfaces of the office interior, but also the sky as visible through the fenestration systems. Reflection by specular surfaces such as the luminaire in the suspended ceiling can contribute to glare if they reflect directional light. The results of the evaluation employing EVALGLARE are listed in Table 8. Detected glare sources are colored in Fig. 19. Since a task area cannot be defined for the given view, a fixed threshold of 2000 cd m^{-2} was applied to the pixel values to identify glare sources, and a threshold of 1,000,000 cd m^{-2} to extract peaks such as reflections of the sun disk.

Discomfort glare as predicted by the DGP is extremely high for case B. The predicted value of 0.896 exceeds the defined range of the metric, and is clearly above the upper limit of tolerable glare defined as 0.45. For cases *A* and *C*, the computed DGPs are in the valid range of 0.2–0.8. The prediction for case A is below, case *C* just above the threshold of 0.35 for perceptible glare. According the DGP, good visual comfort conditions in terms of discomfort are maintained by both diffuse and the retro-reflective coating, but the latter is preferable.

The assessment based on DGI contradicts the predictions by the DGP metric. The result for cases *A* and *C* are in the acceptable range 22–24 with case *C* achieving a minimally better result. Case *B* is clearly higher and must be considered intolerable according to the metric.

The disagreement of the two metrics in rating cases *A* and *C* can be explained by the role of E_v in DGP, and the background luminance L_b in DGI, to account for adaption effects. DGI models adaption based on background luminance L_b, which excludes the glare sources. This favors case *C* where L_b is more than three times higher than in case *A*. The approach is questionable in cases where the glare source covers a large fraction of the field of view, but is not considered to effect adaption. The formulation of DGP, driven by this short-coming, relies on E_v (including the potential glare sources) both as a factor for adaption and a source for discomfort glare.

4. Conclusion

A novel extension to a scanning gonio-photometer for the measurement of retro-reflection has been developed. Applicability and validity of the approach, employing two beam-splitters to compensate for its wavelength dependent transmission and reflection properties, were demonstrated. Based on these initial tests, a fully functional setup shall be developed that reduces error due to misalignment compared to the presented prototype.

The evaluated coating achieves a highly directional, retro-reflective effect. This property is confirmed in both evaluated wavelength ranges Vis and NIr and over a wide range of incident directions $\theta_i = 5–70°$.

Compiled from measured BSDF, the data-driven reflection model in RADIANCE is capable to accurately replicate all characteristic features of the sample. Since RADIANCE implements an advanced algorithm for interpolation, but has no means to extrapolate, the applicability of the model is limited to the range of measured incident directions. Based on the results of this work, the presented apparatus to measure retro-reflection shall be modified accordingly so that a wider range of incident directions can be covered. Yet, the measurement of reflection for incident directions close to grazing is inherently limited. The implementation of an extrapolation algorithm that predicts peaks either in the forward mirror direction or the direction of ideal retro-reflection based on a given set of measurements remains a challenge to overcome limitations of the data-driven model.

Since the retro-reflective effect is achieved independently from the profile geometry, the coating allows to develop Venetian blinds with low profile height. Effective sun-shading could be demonstrated in the comparison with diffuse and specular blinds even with flat, horizontal slats. Since most incident sunlight is directionally reflected toward the outside, visible light is blocked and solar gains are minimized. The application of the coating in future Venetian blinds assemblies promises to achieve high performance as a sun-shading device while maintaining view to the outside.

This study focuses on the effect of the coating rather than the performance of a complete fenestration system. Further research shall assess the performance of the coating when applied in realistic cases with optimized blinds profiles. Different strategies to set the inclination angle of the blinds to maximize view-through and daylight supply shall be tested over extended time-spans employing CBDM.

Role of the funding sources

This research was supported by the doctoral funding scheme of Lucerne University of Applied Sciences and Arts, by the Swiss

Commission for Technology and Innovation CTI within the SCCER FEEB&D (contract #1155000149), and by the Swiss Federal Office of Energy SFOE (#SI501427-01) as part of the project "High Resolution Complex Glazing Library (BIMSOL)". Sole responsibility for content and conclusions lies with the authors.

Pellini S.p.A. as a collaborator within the BIMSOL project provided the sample and funding to cover the measurements.

Acknowledgements

I thank Tuğçe Kazanasmaz and Stephen Wittkopf, who, as supervisor and co-supervisor of my PhD research at Izmir Institute of Technology, were reviewing the work.

Further thanks to Peter Apian-Bennewitz and my colleague Marek Krehel for critical but always encouraging discussions, to Jan Wienold for his patient support in the usage of EVALGLARE, and to Andreas Noback who prepared Fig. 7.

References

[1] S. Darula, J. Christoffersen, M. Malikova, Sunlight and insolation of building interiors, Energy Proc. 78 (2015) 1245–1250, http://dx.doi.org/10.1016/j.egypro.2015.11.266.
[2] S. Hoffmann, E.S. Lee, A. McNeil, L. Fernandes, D. Vidanovic, A. Thanachareonkit, Balancing daylight, glare, and energy-efficiency goals: an evaluation of exterior coplanar shading systems using complex fenestration modeling tools, Energy Build. 112 (2016) 279–298, http://dx.doi.org/10.1016/j.enbuild.2015.12.009.
[3] K. Konis, S. Selkowitz, Effective Daylighting with High-Performance Facades: Emerging Design Practices, Springer, 2017, http://dx.doi.org/10.1007/978-3-319-39463-3.
[4] T. Kolås, Performance of Daylight Redirecting Venetian Blinds for Sidelighted Spaces at High Latitudes (Ph.D. thesis), Norges Teknisk-Naturvitenskapelige Universitet, Fakultet for Arkitektur og Billedkunst, 2013.
[5] H. Köster, Daylight Modulation, Witag-Verlag, 2015.
[6] A.V. Arecchi, T. Messadi, R.J. Koshel, Field Guide to Illumination, SPIE Optical Engineering Press, Bellingham, WA, 2007.
[7] A. Tsangrassoulis, Shading and Daylight Systems, Springer International Publishing, Cham, 2016, pp. 437–466, http://dx.doi.org/10.1007/978-3-319-20831-2_21.
[8] I.L. Wong, A review of daylighting design and implementation in buildings, Renew. Sustain. Energy Rev. 74 (2017) 959–968, http://dx.doi.org/10.1016/j.rser.2017.03.061.
[9] H. Köster, Dynamic daylighting architecture: basics, systems, projects, Springer Sci. Bus. Media (2004).
[10] T.E. Kuhn, State of the art of advanced solar control devices for buildings, Sol. Energy 154 (2017) 112–133, http://dx.doi.org/10.1016/j.solener.2016.12.044.
[11] F. Rossi, A.L. Pisello, A. Nicolini, M. Filipponi, M. Palombo, Analysis of retro-reflective surfaces for urban heat island mitigation: a new analytical model, Appl. Energy 114 (2014) 621–631, http://dx.doi.org/10.1016/j.apenergy.2013.10.038.
[12] H. Sakai, H. Iyota, Development of two new types of retroreflective materials as countermeasures to urban heat islands, Int. J. Thermophys. 38 (9) (2017) 131, http://dx.doi.org/10.1007/s10765-017-2266-y.
[13] M. Ichinose, T. Inoue, T. Nagahama, Effect of retro-reflecting transparent window on anthropogenic urban heat balance, Energy Build. 157 (2017) 157–165, http://dx.doi.org/10.1016/j.enbuild.2017.01.051.
[14] D.M.G. Papaiz Luca, G.L. Oliver, Modeling and measuring of solar shading with retro-reflection microstructure, 15th International Radiance Workshop (2016).
[15] A. Noback, L.O. Grobe, S. Wittkopf, Accordance of light scattering from design and de-facto variants of a daylight redirecting component, Buildings 6 (3) (2016) 30, http://dx.doi.org/10.3390/buildings6030030.
[16] J. Yuan, K. Emura, C. Farnham, A method to measure retro-reflectance and durability of retro-reflective materials for building outer walls, J. Build. Phys. 38 (6) (2015) 500–516, http://dx.doi.org/10.1177/1744259113517208.
[17] F.E. Nicodemus, J.C. Richmond, J.J. Hsia, I.W. Ginsberg, T. Limperis, Geometrical Considerations and Nomenclature for Reflectance, Tech. Rep., US Department of Commerce, National Bureau of Standards, Washington, DC, USA, 1977.
[18] ASTM E2387-05, Standard Practice for Goniometric Optical Scatter Measurements, ASTM International, 2005.
[19] P. Apian-Bennewitz, New scanning gonio-photometer for extended BRTF measurements, in: Proceedings SPIE, Vol. 7792 Reflection, Scattering, and Diffraction from Surfaces II, International Society for Optics and Photonics, Brussels, 2010, pp. 77920, http://dx.doi.org/10.1117/12.860889.
[20] B. Karamata, M. Andersen, Origin and nature of measurement bias in catadioptric parallel goniophotometers, J. Opt. Soc. Am. A 31 (5) (2014) 1040–1048, http://dx.doi.org/10.1364/JOSAA.31.001040.
[21] F. Sametoglu, O. Celikel, Establishment of a computer-controlled retroreflection measurement facility to characterize photometric properties of retroreflectors, Measurement 42 (5) (2009) 757–763, http://dx.doi.org/10.1016/j.measurement.2008.12.007.
[22] A. Rabal, A. Ferrero, J. Campos, J. Fontecha, A. Pons, A. Rubiño, A. Corróns, Automatic gonio-spectrophotometer for the absolute measurement of the spectral BRDF at in-and out-of-plane and retroreflection geometries, Metrologia 49 (3) (2012) 213, http://dx.doi.org/10.1088/0026-1394/49/3/213.
[23] J.C. Stover, Optical Scattering: Measurement and Analysis, 2nd ed., SPIE Optical Engineering Press, Bellingham, WA, 1995.
[24] H. Luo, C. Yuan, Research on cant characteristics of retroreflective film based on laminae combination technology, Opt. Int. J. Light Electr. Opt. 126 (23) (2015) 4272–4277, http://dx.doi.org/10.1016/j.ijleo.2015.08.135.
[25] M. Krehel, L.O. Grobe, S. Wittkopf, A hybrid data-driven BSDF model to predict light transmission trough complex fenestration systems including high incident directions, J. Facade Des. Eng. 4 (3–4) (2016) 79–89, http://dx.doi.org/10.3233/FDE-161191.
[26] K.M. Yoo, G.C. Tang, R.R. Alfano, Coherent backscattering of light from biological tissues, Appl. Opt. 29 (22) (1990) 3237–3239, http://dx.doi.org/10.1364/AO.29.003237.
[27] T. Grosges, Retro-reflection of glass beads for traffic road stripe paints, Opt. Mater. 30 (10) (2008) 1549–1554, http://dx.doi.org/10.1016/j.optmat.2007.09.010.
[28] C. Bourlier, G. Berginc, Multiple scattering in the high-frequency limit with second-order shadowing function from 2D anisotropic rough dielectric surfaces: I. Theoretical study, Waves Random Media 14 (3) (2004) 229–252, http://dx.doi.org/10.1088/0959-7174/14/3/003.
[29] C. Bourlier, G. Berginc, Multiple scattering in the high-frequency limit with second-order shadowing function from 2D anisotropic rough dielectric surfaces: II. Comparison with numerical results, Waves Random Media 14 (3) (2004) 253–276, http://dx.doi.org/10.1088/0959-7174/14/3/004.
[30] L. Belcour, R. Pacanowski, M. Delahaie, A. Laville-Geay, L. Eupherte, Bidirectional reflectance distribution function measurements and analysis of retroreflective materials, J. Opt. Soc. Am. A 31 (12) (2014) 2561–2572, http://dx.doi.org/10.1364/JOSAA.31.002561.
[31] R. Pacanowski, O.S. Celis, C. Schlick, X. Granier, P. Poulin, A. Cuyt, Rational BRDF, IEEE Trans. Visual. Comput. Graph. 18 (11) (2012) 1824–1835, http://dx.doi.org/10.1109/TVCG.2012.73.
[32] L. Claustres, Y. Boucher, M. Paulin, Wavelet-based modeling of spectral Bidirectional Reflectance Distribution Function data, Opt. Eng. 43 (10) (2004) 2327–2339, http://dx.doi.org/10.1117/1.1789138.
[33] W. Jakob, E. d'Eon, O. Jakob, S. Marschner, A comprehensive framework for rendering layered materials, ACM Trans. Graph. 33 (4) (2014) 118:1–118:14, http://dx.doi.org/10.1145/2601097.2601139.
[34] N.L. Jones, C.F. Reinhart, Experimental validation of ray tracing as a means of image-based visual discomfort prediction, Build. Environ. 113 (2017) 131–150, http://dx.doi.org/10.1016/j.buildenv.2016.08.023.
[35] G. Ward, M. Kurt, N. Bonneel, A Practical Framework for Sharing and Rendering Real-World Bidirectional Scattering Distribution Functions, Tech. Rep., Lawrence Berkeley National Laboratory, 2012.
[36] G. Ward, M. Kurt, N. Bonneel, Reducing anisotropic BSDF measurement to common practice, in: R. Klein, H. Rushmeier (Eds.), Eurographics Workshop on Material Appearance Modeling, The Eurographics Association, 2014, http://dx.doi.org/10.2312/mam.20141292.
[37] P. Shirley, K. Chiu, A low distortion map between disk and square, J. Graph. Tools 2 (3) (1997) 45–52, http://dx.doi.org/10.1080/10867651.1997.10487479.
[38] L.O. Grobe, Computational combination of the optical properties of fenestration layers at high directional resolution, Buildings 7 (1) (2017) 22, http://dx.doi.org/10.3390/buildings7010022.
[39] N. Bonneel, M. Van De Panne, S. Paris, W. Heidrich, Displacement interpolation using Lagrangian mass transport ACM Transactions on Graphics (TOG), vol. 30, ACM, 2011, pp. 158, http://dx.doi.org/10.1145/2070781.2024192.
[40] L.O. Grobe, S. Wittkopf, Z.T. Kazanasmaz, High-resolution data-driven models of daylight redirection components, J. Facade Des. Eng. 5 (2) (2017) 101–113, http://dx.doi.org/10.7480/jfde.2017.2.1743.
[41] P. Apian-Bennewitz, Scanning gonio-photometers for asymmetric acquisition of fine-structured BSDF, in: Eurographics 2014 Workshop on Material Appearance Modeling: Issues and Acquisition, MAM '14, Eurographics Association, Aire-la-Ville, Switzerland, 2014, pp. 1–4, http://dx.doi.org/10.2312/mam.20141291.
[42] R. Mitchell, C. Kohler, J. Klems, M. Rubin, D. Arasteh, C. Huizenga, T. Yu, D. Curcija, Window 6.2/Therm 6.2 Research Version User Manual. Tech. Rep. LBNL-941, Lawrence Berkeley National Laboratory, Berkeley, CA, 2008.
[43] R. Schregle, L.O. Grobe, S. Wittkopf, An out-of-core photon mapping approach to daylight coefficients, J. Build. Perform. Simul. 9 (6) (2016) 620–632, http://dx.doi.org/10.1080/19401493.2016.1177116.
[44] J. Wienold, J. Christoffersen, Evaluation methods and development of a new glare prediction model for daylight environments with the use of CCD cameras, Energy Build. 38 (7) (2006) 743–757, http://dx.doi.org/10.1016/j.enbuild.2006.03.017.
[45] J.A. Jakubiec, C.F. Reinhart, The adaptive zone – a concept for assessing discomfort glare throughout daylit spaces, Light. Res. Technol. 44 (2) (2012) 149–170, http://dx.doi.org/10.1177/1477153511420097.